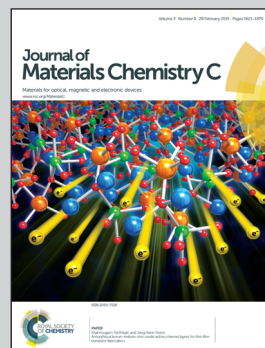


Showcasing research from the State Key Lab of Metal Matrix Composites, Shanghai Jiao Tong University, China.

Title: Coupling of plasmon and 3D antireflection quasi-photonic crystal structure for enhancement infrared absorption

A carbon-matrix Ag wing with a hierarchical sub-micron antireflection quasi-photonic crystal structure (HSAS) was fabricated, which achieved plasmon and coherent coupling between adjacent resonant systems integrated with HSAS.

As featured in:



See Wang Zhang, Di Zhang et al.,  
*J. Mater. Chem. C*, 2015, **3**, 1672.



[www.rsc.org/MaterialsC](http://www.rsc.org/MaterialsC)

Registered charity number: 207890



Cite this: *J. Mater. Chem. C*, 2015, 3, 1672

## Coupling of plasmon and 3D antireflection quasi-photonic crystal structure for enhancement infrared absorption

Junlong Tian,<sup>a</sup> Wang Zhang,<sup>\*a</sup> Xiaotian Fang,<sup>a</sup> Qinglei Liu,<sup>a</sup> Jiajun Gu,<sup>a</sup> Tao Deng,<sup>a</sup> Yuhua Wang<sup>b</sup> and Di Zhang<sup>\*a</sup>

In this study, the carbon-matrix Ag wing with a hierarchical sub-micron antireflection quasi-photonic crystal structure (HSAS) was fabricated by a simple and promising method. This method combines chemosynthesis with biomimetic techniques, without the requirement of expensive equipment and energy intensive processes. Here, the *Troides helena* (Linnaeus) (*T. helena*) forewing (T\_FW) was chosen as the biomimetic template. The carbon-matrix Ag butterfly wing (Ag@C\_T\_FW) achieves a drastically enhanced infrared absorption over a broad spectral range, especially, over the near infrared region. Here, we report methods to enhance and modify the plasmonic resonances in such structures by strongly coupling plasmonic resonances to HSAS. Using the finite difference time domain (FDTD) method, the absorption spectra and the distribution of the energy density near the Ag NPs surface were simulated. Based on the experiment and simulation results, these findings demonstrate that the enhanced infrared absorption over a broad spectral range is due to the mechanism that the plasmon and the coherent coupling between adjacent resonance systems integrate with the HSAS.

Received 5th November 2014  
Accepted 19th November 2014

DOI: 10.1039/c4tc02519a

www.rsc.org/MaterialsC

## Introduction

The resonance excitation of plasmons in metallic nanostructures can provide large electromagnetic enhancements on the surfaces of metals.<sup>1,2</sup> Such field enhancement can be exploited for wide-ranging applications in the sensing,<sup>3–5</sup> enhancing spectral signals,<sup>6</sup> probing catalytic reactions,<sup>7</sup> photothermal therapy,<sup>6,8,9</sup> surface enhanced Raman scattering,<sup>10–13</sup> surface enhanced visible spectra absorption<sup>14–17</sup> and surface enhanced infrared (IR) absorption.<sup>18–21</sup> However, compared with other applications, the application of surface enhanced IR absorption attracted less attention due to the limitations in designing and fabricating nanostructures with reproducible tunable plasmon resonances across a broadband IR region.<sup>22–25</sup> The maximum electromagnetic enhancement in a plasmonic nanostructure occurs for resonance excitations of the plasmons, which are typically found in the visible light and ultraviolet light regions. However, the plasmon resonances are tunable because the plasmon resonances of metallic nanoparticles are strongly dependent on structure and composition.<sup>26</sup> Thus, the plasmon resonance is tuned over a wide spectral region, particularly in the near infrared (NIR)

region.<sup>27,28</sup> Furthermore, the plasmon resonances can also be tuned by modifying the plasmonic interactions that include the plasmonic interactions among the adjacent resonance systems<sup>22</sup> and the plasmonic interactions between the plasmonic components and structure.<sup>29</sup> As of yet, many works have integrated plasmonic components into corresponding functional structures to create, enhance or tailor the properties of materials.<sup>29–32</sup> However, self-assembly of these so-called plasmon resonance nanoparticles (NPs) into thin films and bulk materials on a macro-scale, particularly with related functional sub-micron structures, is difficult when using conventional technologies, such as spontaneous epitaxial nucleation, chemosynthesis, growth of a second and third component onto seed NPs and the convective assisted capillary force assembly method.<sup>30,33–36</sup>

In order to integrate plasmonic components into a 3D sub-micron antireflection quasi-photonic crystal structure (HSAS) to enhance and modify the plasmonic resonances in such structures, in this paper, the carbon-matrix Ag wing (Ag@C\_T\_FW) with HSAS was fabricated by a simple, cost-effective and promising method. This method combines chemosynthesis and biomimetic techniques using the *T. helena* (Linnaeus) forewing (T\_FW) as the biomimetic template. This is because the black forewing of the *T. helena* exhibits strong absorption of visible light through the coupling effect of the melanin/chitin composite and the HSAS of its scales.<sup>37–39</sup> In order to illustrate the mechanism that the plasmon and the coherent coupling between adjacent resonance systems integrate with the HSAS to

<sup>a</sup>State Key Laboratory of Metal Matrix Composites, Shanghai Jiao Tong University, 800 Dongchuan Road, Shanghai, 200240, P. R. China. E-mail: wangzhang@sjtu.edu.cn; zhangdi@sjtu.edu.cn; Fax: +86-21-34202749; Tel: +86-21-34202634

<sup>b</sup>Department of Prosthodontics, Shanghai Jiao Tong University, 800 Dongchuan Road, Shanghai, 200240, P. R. China

enhance IR absorption over a broad spectral range, we systematically studied the optical absorption properties and the distribution of the energy density of the Ag nanosphere array, T\_FW, Ag wing (Ag\_T\_FW) and Ag@C\_T\_FW by experimentation and the finite difference time domain (FDTD) simulation analysis. Based on the experimental and simulation analysis, these results demonstrated that the Ag@C\_T\_FW and Ag\_T\_FW possessed enhancement broadband light absorption, specifically in the IR regions. The reason is that Ag@C\_T\_FW and Ag\_T\_FW integrated plasmon into HSAS. Consequently, the work successfully provides a new route that couples plasmonic resonances to HSAS to enhance broadband IR absorption and utilize the solar energy in the IR range at a lower cost. This appears to be useful in applications of plasmon for optoelectronics, photovoltaics, photothermal and related technologies.

## Experimental section and simulation

### Materials

*T. helena* butterflies were obtained from Shanghai Natural Wild-Insect Kingdom Co. Ltd. Absolute ethanol (EA, 97%) was purchased from Changshu Yangyuan Chemical Co. Ltd. Nitric acid (NA, 67%), ethylenediamine (ED, 99%), silver nitrate (AgNO<sub>3</sub>), ammonium hydroxide (NH<sub>3</sub>·H<sub>2</sub>O) and potassium sodium tartrate were purchased from Sinopharm Chemical Reagent Co. Ltd. All of these compounds were analytically pure and were used as received without further purification.

### Characterization

Characterization using a scanning electron microscope (SEM) was performed on a 20 kV field emission SEM (FESEM) instrument (Quanta 250, FEI, Hillsboro, OR, USA). X-Ray diffraction measurements were conducted using a Rigaku D/max-2550 instrument equipped with a Cu-K $\alpha$  radiation source (Rigaku Corp., Tokyo, Japan). A transmission electron microscope (TEM), high resolution transmission electron microscope (HRTEM) and selected area electron diffraction (SAED) measurements were performed on a JEM-2100F transmission electron microscope (JEOL, Peabody, MA, USA) operating at an acceleration voltage of 200 kV. The absorption over the wavelength range of 300–2500 nm was measured using a Lambda 750 UV-vis-NIR spectrophotometer (PerkinElmer, Waltham, MA, USA). The samples were mounted for UV-vis-NIR spectroscopy using the clip directly located behind the integrating sphere without any substrates. The IR absorption over the wavelength range of 2.5–15  $\mu$ m was measured by Nicolet 6700 (Thermo Fisher Scientific) Fourier transform infrared spectroscopy (FTIR).

### Fabrication of Ag@C\_T\_FW

The procedure of fabricating the Ag@C\_T\_FW includes two steps (Fig. 1). First, to prepare the Ag butterfly wing (Ag\_T\_FW), T\_FW were first immersed in dilute 8 vol% nitric acid for 2 h and then washed in deionized water. The wings were then immersed into an ethanol solution of ethanediamine (25 vol%) for 6 h to obtain the aminated T\_FW and then washed with

ethanol and deionized water. In succession, the aminated T\_FW was immersed into the electroless plating solutions and was followed by standard electroless deposition of Ag NPs onto the T\_FW. The deposition was performed over a period of 15 min and then rinsed with deionized water and dried in a vacuum drying oven at 25 °C in order to prevent these Ag wings from being oxidized. The electroless plating solution is composed of silver nitrate (1 g), ammonium hydroxide (2 mL), potassium sodium tartrate (5 g) and deionized water (100 mL).<sup>12</sup> Compared with the previous work for versatile fabrication of metallic butterfly wings,<sup>12</sup> to eliminate the interference from the plasmon resonance of Au NPs, we did not form the Au nanoparticle (NP) seeds on the aminated bio-surface to fabricate the Au-NP-functionalized butterfly wings. All immersions were placed in a thermostatic waterbath at 25 °C. Second, carbonization of the Ag\_T\_FW using a vacuum tube furnace heated to 450 °C at 3 °C min<sup>-1</sup> was performed for 2 h under vacuum conditions to produce the final Ag@C\_T\_FW.

### Finite difference time domain method

The detailed FDTD model of the Ag nanospheres array (Ag), addition of the Ag nanospheres array to the surface of chitin sheet (Ag\_chitin), T\_FW and Ag\_T\_FW are shown in Fig. 2. All simulations are performed under normal incident light with the plane wave light source laid above the ridges at a distance of 500 nm, and the red arrow represents the incidence direction of the light. The reflection (*R*) monitor is located behind the light source at a distance of 500 nm. The transmission (*T*) monitor is located 100 nm beneath the model (Fig. 2(d)). The absorption is deduced from  $A = 1 - T - R$ . The boundary condition in the *y* directions is periodic (periodic boundary condition, PBC) and in *x* direction is absorbing (perfectly matched layer, PML). The span of *z* direction is zero. Here, in our simulation, the complex permittivity index of the Ag and chitin are provided by the material database of the Optiwave and the reported results,<sup>38</sup> respectively. In order to be consistent with the diameter of the Ag NPs deposited on the surface of the HSAS of Ag@C\_T\_FW as shown in Fig. 4(c) and (d), the diameter of the Ag nanosphere is set to 20 nm. The dimensions of d<sub>1</sub>–d<sub>8</sub> and  $\theta$  were offered in Table 1, which are based on careful observation and statistical analysis of several SEM and TEM images of T\_FW (Fig. 2(e)–(h)). The mesh size was chosen to obtain a good tradeoff between the computer memory required and the simulation time, while ensuring convergence of the results. A convergence test was carefully performed.

## Results and discussion

The deposition of Ag NPs onto the butterfly wing was examined by XRD measurements. As revealed by the XRD results in Fig. 3, the diffraction peaks of Ag\_T\_FW and Ag@C\_T\_FW with  $2\theta$  values of 38°, 44°, 64°, 77° and 81° are assigned to the (111), (200), (220), (311) and (222) planes of cubic phase Ag, respectively (JCPDS card no. 04-0783, silver-3C, syn). The well-defined peaks in the XRD pattern indicate the formation of cubic phase Ag nanoparticles with high crystallinity. In Fig. 3(b), a broad





Fig. 1 Schematic representation of the procedure of fabricating the Ag@C\_T\_FW by electroless deposition and carbonization.

peak located near  $2\theta = 20^\circ$  corresponds to the amorphous carbon. These results confirm the successful fabrication of Ag\_T\_FW and Ag@C\_T\_FW.

The morphologies of the Ag butterfly wings and the carbon-matrix Ag butterfly wings were characterized using FESEM and TEM (Fig. 4). As showed in Fig. 4(a), the Ag nanoparticles were deposited and agglomerated into thin metal film on the ridges and ribs of the T\_FW, when the electroless plating time lasted for 15 min (Ag\_T\_FW). Moreover, the parallel periodic triangular roof-type ridges, nanoscale ribs and windows of the T\_FW were well maintained. The triangular roof-type ridges focus the light into the scale interior *via* multiple antireflections and form the HSAS. That structure facilitates capture of the light. Declining microribs run down the sides of the ridge that induces the internal light-scattering, which assists in trapping light. Staggered windows are present between every two ridges. The windows elongate the light path length and enlarge the energy density distribution interspace, which implies a potentially important linkage with light-harvesting capacity. The ridges, microribs and windows construct the HSAS. After carbonizing the Ag\_T\_FW, the morphologies of the Ag@C\_T\_FW almost do not change, basically, compared with the Ag\_T\_FW, and the HSAS was maintained well with effective

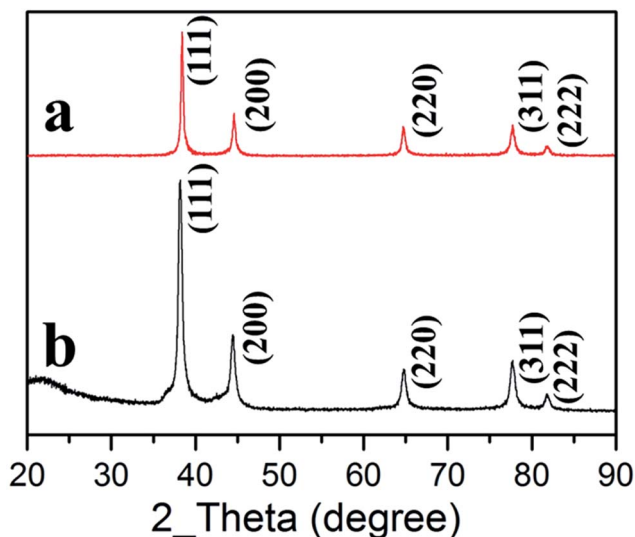


Fig. 3 XRD results of (a) Ag\_T\_FW, (b) Ag@C\_T\_FW.

light absorption performance. Further insight was gained regarding the morphologies and microstructures of the Ag@C\_T\_FW, and the results are shown in Fig. 4(c) and (d). As

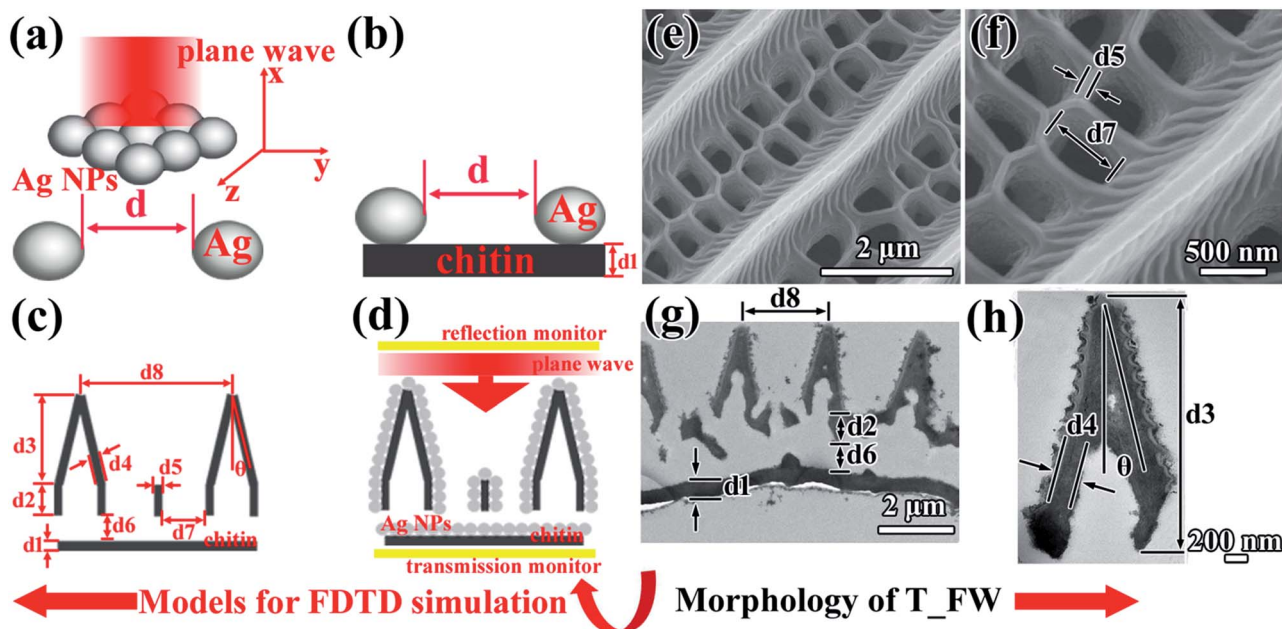


Fig. 2 Models for FDTD simulation of (a) Ag nanosphere array (Ag), (b) added the Ag nanosphere array to the surface of chitin (Ag\_chitin), (c) T\_FW and (d) added the Ag nanosphere array to the surface of T\_FW (Ag\_T\_FW). (e) and (f) SEM images of T\_FW. (g) and (h) TEM images of T\_FW.

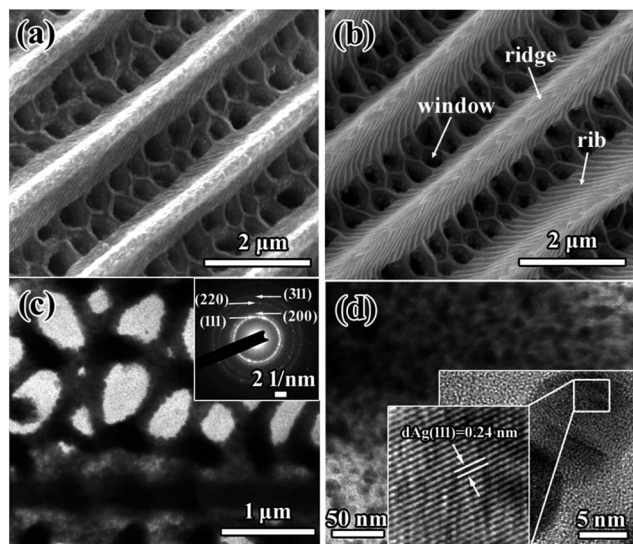


Fig. 4 FESEM images of (a)  $\text{Ag}_\text{T\_FW}$  and (b)  $\text{Ag@C}_\text{T\_FW}$ . (c) and (d) TEM images of  $\text{Ag@C}_\text{T\_FW}$ . The inset of (c) is the SAED image of  $\text{Ag@C}_\text{T\_FW}$ . The inset of (d) is the HRTEM image of  $\text{Ag@C}_\text{T\_FW}$ .

shown in Fig. 4(c), Ag NPs were deposited on the surface of the bio-template and agglomerated into a thin film. The inset of Fig. 4(c) is the SAED image that displays ring and dot patterns, corresponding to the major and minor phases in the product respectively. The clear rings match well with the XRD results, and the relevant planes are indexed as (111), (200), (220) and (311), respectively. The lattice fringes with interplanar distance of  $d_{\text{Ag}(111)} = 0.24$  nm is exhibited in the HRTEM image (Fig. 4(d)).

To explain the mechanism of the enhanced IR absorption over a broadband wavelength region, we compared the absorption properties of the  $\text{Ag@C}_\text{T\_FW}$  with  $\text{Ag}_\text{T\_FW}$ ,  $\text{C}_\text{T\_FW}$  (the carbonized  $\text{T}_\text{FW}$  using the same carbonization process as the  $\text{Ag@C}_\text{T\_FW}$ ),  $\text{T}_\text{FW}$  and BlueTec eta plus\_Cu over the wavelength range of 300–2500 nm (Fig. 5(a)) and 2.5–15  $\mu\text{m}$  (Fig. 5(b)). BlueTec eta plus\_Cu is a commercial absorber that functions as a solar thermal collector. Capable of absorbing extremely high levels of sunlight, BlueTec eta plus\_Cu effectively transforms solar energy into heat (BlueTec GmbH & Co KG, Hesse Germany). As shown in Fig. 5(a), the  $\text{T}_\text{FW}$  shows excellent absorption over the visible light region because of the coupling effect between the melanin/chitin composite and the HSAS of  $\text{T}_\text{FW}$ .<sup>38,39</sup> Compared with the absorption properties of the  $\text{T}_\text{FW}$ , the  $\text{C}_\text{T\_FW}$  provided enhancement in absorption in the IR region, demonstrating that amorphous carbon provides better IR absorption than the melanin/chitin composite of  $\text{T}_\text{FW}$ . These results also show that the enhanced infrared

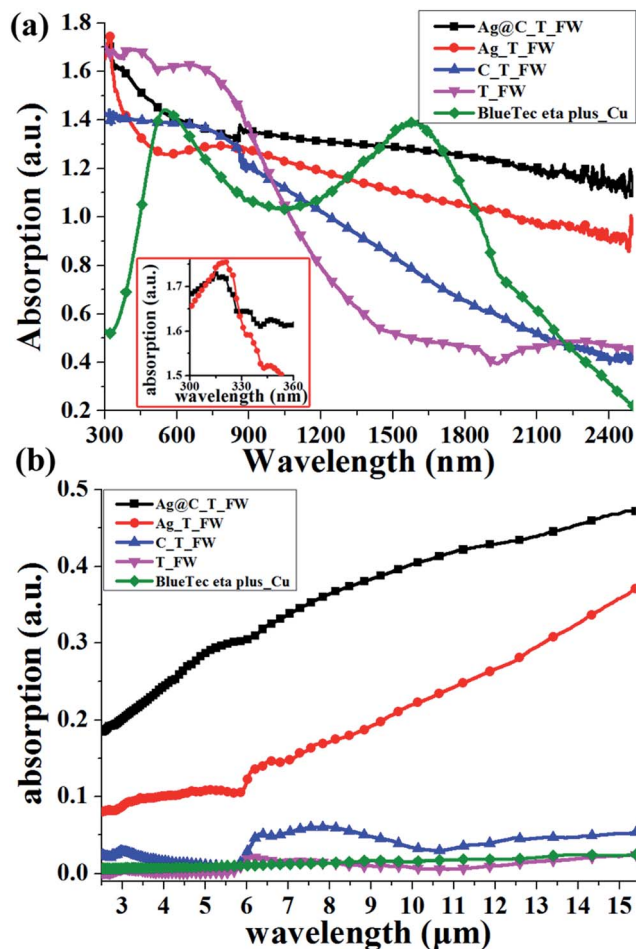


Fig. 5 Absorption spectra of  $\text{Ag@C}_\text{T\_FW}$ ,  $\text{Ag}_\text{T\_FW}$ ,  $\text{C}_\text{T\_FW}$ ,  $\text{T}_\text{FW}$  and BlueTec eta plus\_Cu, (a) over the wavelength range of 300–2500 nm, (b) over the wavelength range of 2.5–15  $\mu\text{m}$ . The inset of Fig. 5(a) is the absorption spectra of  $\text{Ag@C}_\text{T\_FW}$  and  $\text{Ag}_\text{T\_FW}$  over the wavelength range of 300–360 nm with a higher magnification.

absorption property is not only decided by the super absorption structure but also dictated by the absorption properties of materials. As shown in Fig. 5(a) and the inset of Fig. 5(a), the absorption spectra of  $\text{Ag@C}_\text{T\_FW}$  and  $\text{Ag}_\text{T\_FW}$  display the characteristic peak at 312 nm and 318 nm, respectively, which resulted from the Ag NPs plasmon resonance.<sup>40</sup> Over the wavelength region of NIR (Fig. 5(a)) and mid infrared (MIR) (Fig. 5(b)), the  $\text{Ag}_\text{T\_FW}$  exhibits a more intensive absorption, compared with  $\text{C}_\text{T\_FW}$  and  $\text{T}_\text{FW}$ . The reason is that first, the plasmon resonance of the Ag NPs resulted in an enhanced absorption. Second, the coherent coupling between adjacent resonant systems created an enhancement of light absorption over a broadband IR region.<sup>22,41</sup> Furthermore, the plasmon

Table 1 The dimensions of d1–d8 and  $\theta$

	d1 ( $\mu\text{m}$ )	d2 ( $\mu\text{m}$ )	d3 ( $\mu\text{m}$ )	d4 ( $\mu\text{m}$ )	d5 ( $\mu\text{m}$ )	d6 ( $\mu\text{m}$ )	d7 ( $\mu\text{m}$ )	d8 ( $\mu\text{m}$ )	$\theta$ ( $^\circ$ )
Value	0.460	0.900	3.270	0.200	0.200	1.010	0.530	2.870	13.0
Variance	0.003	0.016	0.046	0.001	0.001	0.004	0.003	0.002	—

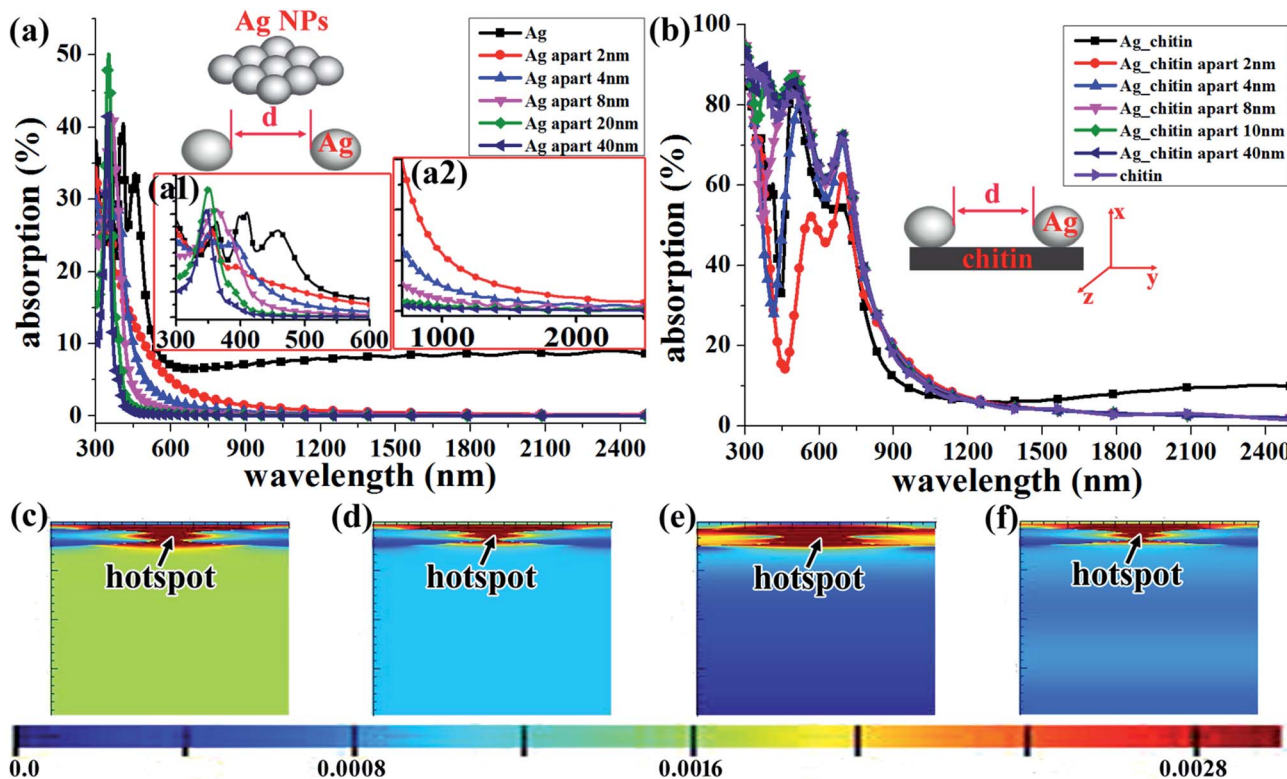


Fig. 6 FDTD simulation results for Ag nanospheres array (Ag) and addition of the Ag nanospheres array to the surface of chitin (Ag\_chitin). (a) The absorption spectra of the Ag with different spacing:  $d = 0$  nm (Ag),  $d = 2$  nm (Ag apart 2 nm),  $d = 4$  nm (Ag apart 4 nm),  $d = 8$  nm (Ag apart 8 nm),  $d = 20$  nm (Ag apart 20 nm) and  $d = 40$  nm (Ag apart 40 nm). (a1) and (a2) is the absorption spectra in the wavelength range of 300–600 nm and 700–2500 nm with a higher magnification, respectively. (b) The absorption spectra of chitin (chitin sheet) and the Ag\_chitin with different spacing:  $d = 0$  nm (Ag\_chitin),  $d = 2$  nm (Ag\_chitin apart 2 nm),  $d = 4$  nm (Ag\_chitin apart 4 nm),  $d = 8$  nm (Ag\_chitin apart 8 nm),  $d = 20$  nm (Ag\_chitin apart 20 nm) and  $d = 40$  nm (Ag\_chitin apart 40 nm). (c) and (d) Maps of the energy flux density amplitude of Ag, in which the incident light is 470 nm and 980 nm, respectively; (e) and (f) maps of the energy flux density amplitude of Ag\_chitin, in which the incident light is 470 nm and 980 nm, respectively.

resonance and the coherent coupling between adjacent resonance systems integrate with the HSAS of T\_FW, which can create the broadband light absorption enhancement with greater intensity. Remarkably, the Ag@C\_T\_FW possesses a more effective broadband light absorption, compared with Ag\_T\_FW, because the carbon matrix is better for infrared absorption compared with the melanin/chitin composite matrix. Consequently, the Ag@C\_T\_FW coupled the plasmonic resonances to carbon-matrix HSAS. By optimizing the coupling among the plasmon, functional structure and the matrix materials, the samples can possess a further enhanced broadband light absorption property. Moreover, the intensive absorption enhancement was achieved over the wavelength range of 2.5–15  $\mu\text{m}$  (Fig. 5(b)). Compared with the BlueTec eta plus\_Cu, the average absorbance intensities of the Ag@C\_T\_FW increased by 42.75% in the wavelength range of 300–2500 nm and was as much as 28.7 times greater in the wavelength range of 2.5–15  $\mu\text{m}$ .

To further demonstrate that the plasmon resonance and the coherent coupling between adjacent resonance systems create an enhancement in absorption over a broadband IR region, the FDTD simulation was used. From Fig. 6(a) and (a1), we can find that in the Ag nanosphere array, when the Ag nanospheres

touched each other exhibits multiple absorbance maxima over the wavelength range of 300–600 nm. While increasing the separation distance of the Ag nanospheres, the multiple absorbance maxima became gradually weaker and finally disappeared. The absorption spectra exhibited only a single peak when the separation distance increased to 40 nm, which were effectively considered as single particles. The first peak, located near the resonance peak of single particles, is attributed to the quadrupole plasmon excitation in the coupled Ag nanospheres, while the other peaks at longer wavelength are attributed to the dipole plasmon resonance of the Ag nanospheres.<sup>42</sup> The multiple absorbance maxima is attributed to the coupling effect of plasmon response of the Ag nanospheres.<sup>31,42,43</sup> The oscillating electrons in one Ag nanosphere experience the electric field due to the oscillations in the adjacent Ag nanospheres, which can lead to a collective plasmon oscillation of the aggregated system.<sup>42</sup> As shown in Fig. 6(a) and (a2), the linked Ag nanospheres array exhibits a more enhanced broadband IR absorption performance compared with the other Ag nanospheres array when the Ag nanospheres are in different spacing. Moreover, the absorptions decreased when gradually increasing the spacing  $d$  of the Ag nanospheres. When adding the Ag nanospheres array to the surface of chitin, the Ag\_chitin



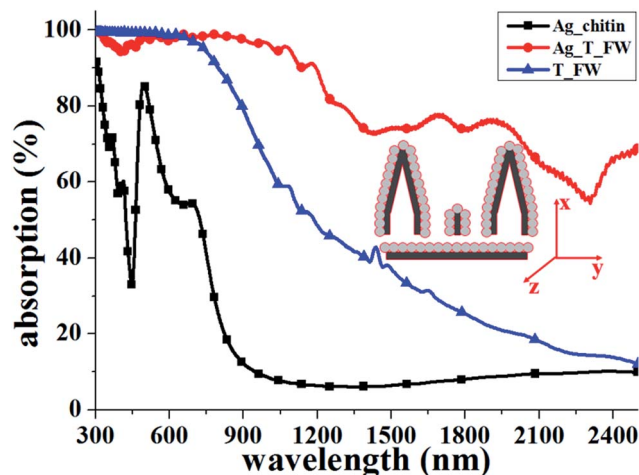


Fig. 7 FDTD calculations for the absorption spectra of Ag\_chitin, Ag\_T\_FW and T\_FW.

possesses similar enhancement absorption performance over a broadband IR region, and the absorption intensity decreased when increasing the spacing  $d$  of the Ag nanospheres. Consequently, the simulation results as shown in Fig. 6(a) and (b) indicate that the coherent coupling between adjacent resonance systems resulted in an enhanced IR absorption over a broadband wavelength region.<sup>22</sup> Furthermore, coherent coupling between adjacent resonance systems is demonstrated by the maps of the energy flux density amplitude. As shown in Fig. 6(c)–(f), the Ag nanospheres efficiently generated plasmons and substantially enhanced the electromagnetic field in the adjacent region between two nanospheres, providing hotspots, especially located in the interparticle region.

To better demonstrate the plasmon resonance and the coherent coupling between adjacent resonance systems integrated with the HSAS of T\_FW, which can create the broadband light absorption enhancement with greater intensity over the IR region, we used the FDTD to calculate the absorption properties of the Ag\_chitin, Ag\_T\_FW and T\_FW (Fig. 7). Compared with the absorption spectra of T\_FW, that of Ag\_T\_FW exhibits an enhancement in absorption over a broadband IR region. Moreover, the absorption intensity of Ag\_T\_FW integrated from 300 nm to 2500 nm exhibits about 1.3 times enhancement compared with absorption intensity of T\_FW. These findings indicate that the plasmon resonance with the coherent coupling between adjacent resonance systems can enhance IR absorption over a broadband. Additionally, compared with the absorption spectra of Ag\_chitin, that of Ag\_T\_FW exhibits a more intensive absorption over the wavelength range over 300–2500 nm, which demonstrates that the plasmon integrates with the HSAS and can achieve an enhanced broadband light absorption. The absorption intensity of Ag\_T\_FW (with HSAS) integrated from 300 nm to 2500 nm exhibits about 4.05 times enhancement compared with absorption intensity of Ag\_chitin (without HSAS). Furthermore, compared with the optical absorption of the HCP Au nanoshell<sup>22</sup> (without HSAS), the Ag\_T\_FW possesses a more intensive optical absorption capability. Consequently,

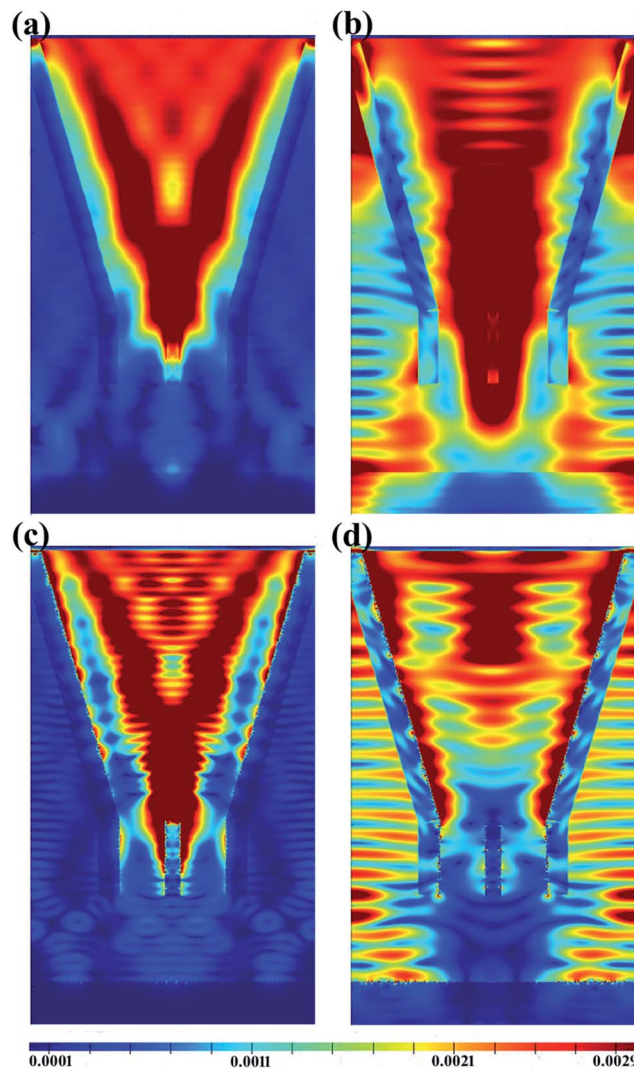


Fig. 8 (a) and (b) Maps of the energy flux density amplitude of T\_FW, in which the incident light is 470 nm and 980 nm, respectively; (c) and (d) maps of the energy flux density amplitude of Ag\_T\_FW, in which the incident light is 470 nm and 980 nm, respectively.

the Ag\_T\_FW caused the plasmon resonance and the coherent coupling between adjacent resonance systems to integrate with the HSAS, creating the broadband light absorption enhancement with greater intensity, specially, over the IR region. Furthermore, the simulation results showing that Ag\_T\_FW exhibited an enhanced broadband IR absorption are in excellent agreement with those experimentally observed as shown in Fig. 5(a) and 7. However, the observed difference in the absorption spectra in the visible light region can be attributed only to monolayer Ag nanospheres covered on the surface of the HSAS for the FDTD simulation model which generated a lower reflection resulting from the monolayer Ag layer. Indeed, for the experimental sample, the multilayer Ag nanospheres covered on the surface of the HSAS of the T\_FW generated a higher reflection compared with the FDTD simulation model.

The plasmon resonance and the coherent coupling between adjacent resonance systems integrated with the HSAS is further

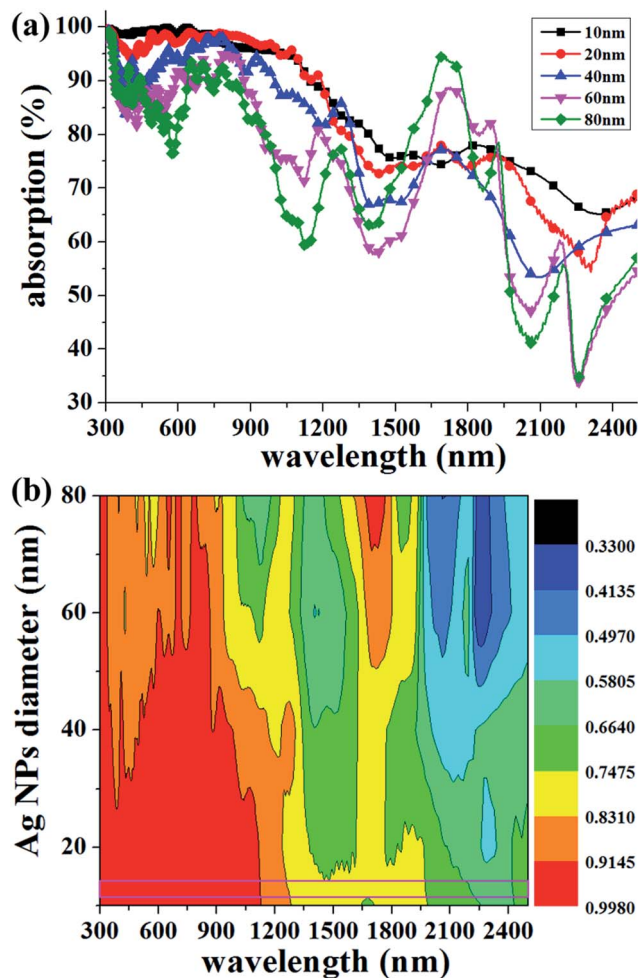


Fig. 9 (a) FDTD calculations for the absorption spectra of Ag<sub>T</sub>\_FW with different Ag NPs' diameters (10 nm, 20 nm, 40 nm, 60 nm and 80 nm), respectively. (b) The simulation of the absorption spectra of Ag<sub>T</sub>\_FW versus Ag NPs diameter.

demonstrated by the maps of the energy flux density amplitude of T<sub>FW</sub> and Ag<sub>T</sub>\_FW, as shown in Fig. 8. The intensive energy density distributed in the region is located in the windows and between the two ridges. These findings demonstrate that the triangular roof type ridges possess a facilitating light capturing capacity because of the antireflection performance of the triangular roof type structure. Interestingly, the obvious hot-spots locate on the surface of the Ag nanospheres layer, which resulted from the plasmon resonance and the coherent coupling between adjacent resonance systems (Fig. 8(c) and (d)). From the energy flux density distribution maps of Ag<sub>T</sub>\_FW, we can come to the conclusion that the Ag<sub>T</sub>\_FW and Ag@C<sub>T</sub>\_FW achieved the plasmon resonance and the coherent coupling between adjacent resonance systems integrated with the HSAS.

In order to optimise the enhancement of the broadband light absorption, the parametric study is carried out taking into account the size of Ag NPs which integrated with the HSAS of T<sub>FW</sub>. By comparing the absorption spectra of Ag<sub>T</sub>\_FW with different Ag NPs' diameters (20 nm, 40 nm, 60 nm and 80 nm),

we can find that the intensity of the light absorption is decreased with increasing the diameter of the Ag NPs, except for the wavelength range located near 1600 nm (Fig. 9(a) and (b)). However, comparing the absorption spectra of Ag<sub>T</sub>\_FW with the Ag NPs' diameter equalling 20 nm, the enhancement of the light absorption of Ag<sub>T</sub>\_FW with the Ag NPs' diameter equaling 10 nm is not significant, especially over the wavelength range located near 838 nm and 1600 nm. As shown in Fig. 9(b), the absorption is more effective over the purple rectangle region which demonstrated that the Ag<sub>T</sub>\_FW with the Ag NPs' diameter equalling 12 to 15 nm possesses more effective light absorption. Consequently, the Ag NPs with suitable size integrated with the HSAS of T<sub>FW</sub> can possess more effective light absorption over a broadband range. These simulation results offer guidance for our further experiments to obtain a more effective light absorption material by controlling the diameter of Ag NPs of the Ag<sub>T</sub>\_FW and Ag@C<sub>T</sub>\_FW with a suitable size.

## Conclusions

In this work, we combined chemosynthesis and biomimetic techniques using the T<sub>FW</sub> as the biomimetic-template to fabricate the Ag@C<sub>T</sub>\_FW with a HSAS without the requirement of expensive equipment and energy intensive processes. The Ag@C<sub>T</sub>\_FW coupled the plasmonic resonances to carbon-based HSAS and achieved a drastically enhanced infrared absorption over a broad spectral range, especially, over the NIR region. However, the enhancement absorption was also obtained in the MIR range. We find that the IR absorption is closely related to the HSAS and the SPR of the Ag nanoparticles. Using the FDTD method, the distribution of the intensive energy density near the Ag NPs surface and the absorption spectra were simulated. Based on the experiment and simulation results, the improvement can be explained that first the plasmon resonance of the Ag NPs resulted in an enhanced absorption. Second, the coherent coupling between adjacent resonance systems created the broadband light absorption enhancement. Furthermore, the plasmon resonance and the coherent coupling between adjacent resonant systems integrate with the HSAS of T<sub>FW</sub>, which can create the broadband light absorption enhancement with greater intensity. Consequently, the Ag@C<sub>T</sub>\_FW provides a new perspective for coupling the plasmon and the coherent coupling between adjacent resonance systems with HSAS. The work successfully provides a new route to enhance broadband infrared absorption and utilize the solar energy in infrared range at lower cost. It also appears to be useful in applications of the plasmon for optoelectronics, photovoltaics, photothermal and related technologies.

## Acknowledgements

This work was supported by the National Natural Science Foundation of China (no. 51202145, no. 51131004 and no. 51171110), the National Basic Research Program of China (973 Program, no. 2011cb922200) and Research Fund for the Doctoral Program of Higher Education of China (20120073120006 and 20120073130001).



## Notes and references

- 1 A. Dmitriev, T. Pakizeh, M. Käll and D. S. Sutherland, *Small*, 2007, **3**, 294–299.
- 2 J. Zhang, Y. Fu, M. H. Chowdhury and J. R. Lakowicz, *Nano Lett.*, 2007, **7**, 2101–2107.
- 3 R. Gordon, D. Sinton, K. L. Kavanagh and A. G. Brolo, *Acc. Chem. Res.*, 2008, **41**, 1049–1057.
- 4 I. A. Larmour and D. Graham, *Analyst*, 2011, **136**, 3831–3853.
- 5 B. Ng, J. Wu, S. M. Hanham, A. I. Fernández-Domínguez, N. Klein, Y. F. Liew, M. B. Breese, M. Hong and S. A. Maier, *Adv. Opt. Mater.*, 2013, **1**, 543–548.
- 6 A. M. Gobin, M. H. Lee, N. J. Halas, W. D. James, R. A. Drezek and J. L. West, *Nano Lett.*, 2007, **7**, 1929–1934.
- 7 E. M. Larsson, C. Langhammer, I. Zorić and B. Kasemo, *Science*, 2009, **326**, 1091–1094.
- 8 M. A. Mackey, M. R. Ali, L. A. Austin, R. D. Near and M. A. El-Sayed, *J. Phys. Chem. B*, 2014, **118**, 1319–1326.
- 9 Y. Ma, X. Liang, S. Tong, G. Bao, Q. Ren and Z. Dai, *Adv. Funct. Mater.*, 2013, **23**, 815–822.
- 10 S. T. Sivapalan, B. M. DeVetter, T. K. Yang, T. van Dijk, M. V. Schulmerich, P. S. Carney, R. Bhargava and C. J. Murphy, *ACS Nano*, 2013, **7**, 2099–2105.
- 11 Y. Tan, J. Gu, L. Xu, X. Zang, D. Liu, W. Zhang, Q. Liu, S. Zhu, H. Su and C. Feng, *Adv. Funct. Mater.*, 2012, **22**, 1578–1585.
- 12 Y. Tan, J. Gu, X. Zang, W. Xu, K. Shi, L. Xu and D. Zhang, *Angew. Chem., Int. Ed.*, 2011, **123**, 8457–8461.
- 13 C. H. Moran, M. Rycenga, X. Xia, C. M. Cobley and Y. Xia, *Nanotechnology*, 2014, **25**, 014007.
- 14 X. Chen, B. Jia, J. K. Saha, B. Cai, N. Stokes, Q. Qiao, Y. Wang, Z. Shi and M. Gu, *Nano Lett.*, 2012, **12**, 2187–2192.
- 15 H. Tan, R. Santbergen, A. H. Smets and M. Zeman, *Nano Lett.*, 2012, **12**, 4070–4076.
- 16 H. A. Atwater and A. Polman, *Nat. Mater.*, 2010, **9**, 205–213.
- 17 V. E. Ferry, J. N. Munday and H. A. Atwater, *Adv. Mater.*, 2010, **22**, 4794–4808.
- 18 T. Jensen, R. Van Duyne, S. Johnson and V. Maroni, *Appl. Spectrosc.*, 2000, **54**, 371–377.
- 19 J. Kundu, F. Le, P. Nordlander and N. J. Halas, *Chem. Phys. Lett.*, 2008, **452**, 115–119.
- 20 K. Ataka, F. Giess, W. Knoll, R. Naumann, S. Haber-Pohlmeier, B. Richter and J. Heberle, *J. Am. Chem. Soc.*, 2004, **126**, 16199–16206.
- 21 C.-W. Cheng, M. N. Abbas, C.-W. Chiu, K.-T. Lai, M.-H. Shih and Y.-C. Chang, *Opt. Express*, 2012, **20**, 10376–10381.
- 22 F. Le, D. W. Brandl, Y. A. Urzhumov, H. Wang, J. Kundu, N. J. Halas, J. Aizpurua and P. Nordlander, *ACS Nano*, 2008, **2**, 707–718.
- 23 T. Wang, V. H. Nguyen, A. Buchenauer, U. Schnakenberg and T. Taubner, *Opt. Express*, 2013, **21**, 9005–9010.
- 24 J. n. M. Hoffmann, X. Yin, J. Richter, A. Hartung, T. W. Maß and T. Taubner, *J. Phys. Chem. C*, 2013, **117**, 11311–11316.
- 25 L. V. Brown, K. Zhao, N. King, H. Sobhani, P. Nordlander and N. J. Halas, *J. Am. Chem. Soc.*, 2013, **135**, 3688–3695.
- 26 H. Wang, D. W. Brandl, P. Nordlander and N. J. Halas, *Acc. Chem. Res.*, 2007, **40**, 53–62.
- 27 S. E. Skrabalak, J. Chen, Y. Sun, X. Lu, L. Au, C. M. Cobley and Y. Xia, *Acc. Chem. Res.*, 2008, **41**, 1587–1595.
- 28 X. Huang, S. Neretina and M. A. El-Sayed, *Adv. Mater.*, 2009, **21**, 4880–4910.
- 29 D. Chanda, K. Shigeta, T. Truong, E. Lui, A. Mihi, M. Schulmerich, P. V. Braun, R. Bhargava and J. A. Rogers, *Nat. Commun.*, 2011, **2**, 479.
- 30 T. Jägeler-Hoheisel, J. Cordeiro, O. Lecarme, A. Cucho, C. Girard, E. Dujardin, D. Peyrade and A. Arbouet, *J. Phys. Chem. C*, 2013, **117**, 23126–23132.
- 31 A. S. Urban, X. Shen, Y. Wang, N. Large, H. Wang, M. W. Knight, P. Nordlander, H. Chen and N. J. Halas, *Nano Lett.*, 2013, **13**, 4399–4403.
- 32 J. Li, M. Hossain, B. Jia, D. Buso and M. Gu, *Opt. Express*, 2010, **18**, 4491–4498.
- 33 X. Huang, S. Tang, B. Liu, B. Ren and N. Zheng, *Adv. Mater.*, 2011, **23**, 3420–3425.
- 34 W. Shi, H. Zeng, Y. Sahoo, T. Y. Ohulchanskyy, Y. Ding, Z. L. Wang, M. Swihart and P. N. Prasad, *Nano Lett.*, 2006, **6**, 875–881.
- 35 Y. Kang, X. Ye and C. B. Murray, *Angew. Chem., Int. Ed.*, 2010, **49**, 6156–6159.
- 36 L. Cheng, C. Ma, G. Yang, H. You and J. Fang, *J. Mater. Chem. A*, 2014, **2**, 4534–4542.
- 37 W. Zhang, D. Zhang, T. Fan, J. Gu, J. Ding, H. Wang, Q. Guo and H. Ogawa, *Chem.*, 2008, **21**, 33–40.
- 38 A. Herman, C. Vandenbem, O. Deparis, P. Simonis and J. P. Vigneron, *Proc. SPIE*, 2011, **8094**, 80940H1–80940H12.
- 39 Q. Zhao, X. Guo, T. Fan, J. Ding, D. Zhang and Q. Guo, *Soft Matter*, 2011, **7**, 11433–11439.
- 40 G. S. Métraux and C. A. Mirkin, *Adv. Mater.*, 2005, **17**, 412–415.
- 41 Z. Ye, S. Chaudhary, P. Kuang and K.-M. Ho, *Opt. Express*, 2012, **20**, 12213–12221.
- 42 S. K. Ghosh and T. Pal, *Chem. Rev.*, 2007, **107**, 4797–4862.
- 43 E. Prodan, C. Radloff, N. Halas and P. Nordlander, *Science*, 2003, **302**, 419–422.